

ACCEPTED MANUSCRIPT

## Multi-resolution progressive computational ghost imaging

To cite this article before publication: cheng zhou *et al* 2019 *J. Opt.* in press <https://doi.org/10.1088/2040-8986/ab1471>

### Manuscript version: Accepted Manuscript

Accepted Manuscript is “the version of the article accepted for publication including all changes made as a result of the peer review process, and which may also include the addition to the article by IOP Publishing of a header, an article ID, a cover sheet and/or an ‘Accepted Manuscript’ watermark, but excluding any other editing, typesetting or other changes made by IOP Publishing and/or its licensors”

This Accepted Manuscript is © 2019 IOP Publishing Ltd.

During the embargo period (the 12 month period from the publication of the Version of Record of this article), the Accepted Manuscript is fully protected by copyright and cannot be reused or reposted elsewhere. As the Version of Record of this article is going to be / has been published on a subscription basis, this Accepted Manuscript is available for reuse under a CC BY-NC-ND 3.0 licence after the 12 month embargo period.

After the embargo period, everyone is permitted to use copy and redistribute this article for non-commercial purposes only, provided that they adhere to all the terms of the licence <https://creativecommons.org/licenses/by-nc-nd/3.0>

Although reasonable endeavours have been taken to obtain all necessary permissions from third parties to include their copyrighted content within this article, their full citation and copyright line may not be present in this Accepted Manuscript version. Before using any content from this article, please refer to the Version of Record on IOPscience once published for full citation and copyright details, as permissions will likely be required. All third party content is fully copyright protected, unless specifically stated otherwise in the figure caption in the Version of Record.

View the [article online](#) for updates and enhancements.

# Multi-resolution Progressive Computational Ghost Imaging

Cheng Zhou<sup>1,2,3</sup>, Tian Tian<sup>4</sup>, Chao Gao<sup>5</sup>, Wenlin Gong<sup>6</sup>,  
and Lijun Song<sup>1,2</sup>

<sup>1</sup> Institute for Interdisciplinary Quantum Information Technology, Jilin Engineering Normal University, Changchun 130052, China

<sup>2</sup> Jilin Engineering Laboratory for Quantum Information Technology, Changchun 130052, China

<sup>3</sup> Center for Quantum Sciences and School of Physics, Northeast Normal University, Changchun 130024, China

<sup>4</sup> School of Science, Changchun University, Changchun 130022, China

<sup>5</sup> Department of Physics, Changchun University of Science and Technology, Changchun 130022, China

<sup>6</sup> Key Laboratory for Quantum Optics and Center for Cold Atom Physics of CAS, Shanghai Institute of Optics and Fine Mechanics, Chinese Academy of Sciences, Shanghai 201800, China

E-mail: gongwl@siom.ac.cn and ccdxslj@126.com

February 2019

**Abstract.** Most studies on ghost imaging focus on high-quality and high-resolution imaging with few measurements. However, as far as we know, continuous multi-resolution imaging is rarely mentioned. In this work, we both theoretically and experimentally demonstrate a method that uses the Hadamard derived pattern to realize continuous multi-resolution imaging simply and quickly, which we call multi-resolution progressive computational ghost imaging, whereby both the reconstruction time and measurements required for multi-resolution images can be significantly reduced. This approach improves the flexibility of ghost imaging, and can be extended to multi-resolution image-dependent practical applications such as target tracking and recognition.

*Keywords:* ghost imaging, multi-resolution imaging, Hadamard derived pattern  
Submitted to: *J. Opt.*

## 1. Introduction

Ghost imaging (GI) is realized by correlating the light field reflected (or transmitted) from the object with the reference light field [1]. Because all the photons transmitted (or reflected) from the object illuminate the same bucket detector and the measurement method is global random, this technique has the superiority of higher sensitivity in detection and higher efficiency in information extraction than traditional optical imaging [2]. And GI has aroused increasing interest in the applications like remote sensing [3, 4, 5], super-resolution [6], optical encryption [7].

In order to simplify the schematic of GI, computational ghost imaging (CGI) that requires only one optical path was theoretically proposed by Shapiro [8] and later was demonstrated by Bromberg [9]. In 2009, Katz et al. introduced compressive sensing into image reconstruction of CGI where better reconstruction result can be obtained by even using the measurement far below Nyquist limit [10]. In order to enhanced the imaging characteristics of compressive GI, most works were focused on the imaging scenes and sparse representation of the targets [11, 12, 13].

Recently, the optimization coding of speckle pattern for GI was considered [14, 15, 16, 17, 18]. These schemes are important ways to reduce the number of measurements, reconstruction time and computing resources. Averbuch et al. [14] proposed a high-performance imaging scheme which directly uses the patterns that form the sparse basis to replace classical random speckle patterns. Then, a more optimized method named compressive adaptive computational ghost imaging (CCGI) was reported by A $\beta$ mann et al. The CCGI scheme can overcome the shortcomings of image restoration is time-consuming and the computation resource required is relatively high [15]. Subsequently, Yu et al. [16] proposed a adaptive compressive ghost imaging (ACGI) scheme, which made total L-level wavelet transform on the image, and produced full screen scattered speckles by using sparse random matrices, whereby the measurements required for any image size can be further reduced. Later, Soldevila et al. [17] pro-

posed another similar method, which is based on smart sampling of the scene with a small set of masks. These masks were adaptively resized when the part of the scene needs to be recorded with higher resolution. More practical, Phillips et al. [18] proposed a framework that exploited the spatiotemporal redundancy of many dynamic scenes. This study recognizes that sometimes there is no need to image the entire field of view in high resolution, but provides patterns enabling the resolution to be continuously tuned across the field of view.

Moreover, Sun et al. [19] proposed a Russian Dolls ordering of the Hadamard basis CGI method in which they optimized the measurement order of the Hadamard matrix, and achieved optimal reconstruction for any truncation of that pattern sequence. Noteworthy, the Hadamard matrix has a significant characteristic that each Hadamard matrix contains within it each lower order Hadamard matrix, and each even order Hadamard matrix can realize a kind of resolution imaging in CGI. If we reorder the hadamard matrix from low to high by even order, the multi-resolution images will be obtained in a set of CGI experimental.

Here, a scheme that combines the advantages of Ref.[19] and the ideas of progressive transmission [20], which we call multi-resolution progressive computational ghost imaging (MPCGI). This scheme has four main advantages: 1). Continuous multi-resolution images can be obtained directly and quickly; 2). The complexity is lower than that of compressive sensing schemes based on wavelet transform, thus it is more suitable for applications that do not require higher multi-resolution imaging such as air surveillance; 3). The ordering of Hadamard derived pattern can be significantly fewer than ‘Russian Dolls’ ordering [19]; 4). We overcome the difficulty of determining the spatial resolution.

The rest of the paper is organized as follows. In section 2, we review the Hadamard transformation and propose the scheme of multi-resolution progressive imaging utilizing the Hadamard derived pattern. In section 3, we demonstrate our experiment by taking the airplane model as a target object and discuss

ACCEPTED

the effect of detection signal-to-noise ratio. In section 4, the conclusion is made.

## 2. Theoretical analysis

The schematic diagram of CGI is presented in Fig. 1. A projector as the light modulator projects the modulated light field onto an object with a reflection coefficient  $O(x, y)$ . The total reflected signals are collected by a bucket detector. The  $m$ th light field and bucket signal are expressed as  $I^{(m)}(x, y)$ ,  $B^{(m)}$ , respectively.

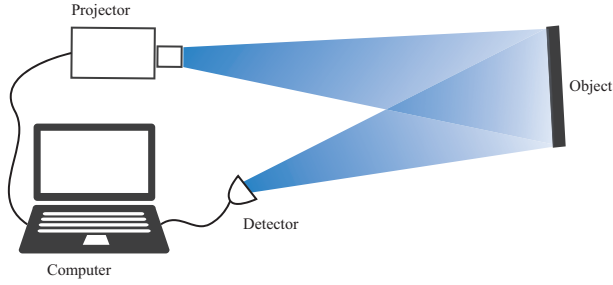


Figure 1. (Color online) Schematic diagram of computational ghost imaging.

### 2.1. Theory of image reconstruction

In conventional GI, the reflected coefficient can be obtained by computing the correlation between  $I^{(m)}(x, y)$  and  $B^{(m)}$

$$O_{\text{GI}}(x, y) = \frac{1}{M} \sum_{m=1}^M [(B^{(m)} - \langle B^{(m)} \rangle) \cdot (I^{(m)}(x, y) - \langle I^{(m)}(x, y) \rangle)], \quad (1)$$

where  $\langle B^{(m)} \rangle = \frac{1}{M} \sum_{m=1}^M B^{(m)}$  and  $\langle I^{(m)}(x, y) \rangle = \frac{1}{M} \sum_{m=1}^M I^{(m)}(x, y)$ . We can transform the  $I^{(m)}(x, y)$  (dimensions  $p \times q$ ) of  $M$  measurements into a matrix form

$$\Phi = \begin{bmatrix} I^{(1)}(1, 1) & I^{(1)}(1, 2) & \cdots & I^{(1)}(p, q) \\ I^{(2)}(1, 1) & I^{(2)}(1, 2) & \cdots & I^{(2)}(p, q) \\ \vdots & \vdots & \ddots & \vdots \\ I^{(M)}(1, 1) & I^{(M)}(1, 2) & \cdots & I^{(M)}(p, q) \end{bmatrix}. \quad (2)$$

Here, each row of the matrix  $\Phi$  is converted from a row vector of length  $p \times q$ , which is obtained by reshaping the  $m$ th light field  $I^{(m)}(x, y)$ .

Thus, Eq. 1 can be rewritten into a matrix form

$$\begin{aligned} O_{\text{GI}}(x, y) &= \frac{1}{M} (\Phi - I\langle\Phi\rangle)^T (B - I\langle B\rangle) \\ &= \frac{1}{M} (\Phi - I\langle\Phi\rangle)^T (\Phi - I\langle\Phi\rangle) \mathbf{O} \\ &= \frac{1}{M} \Psi^T \Psi \mathbf{O}, \end{aligned} \quad (3)$$

where,  $\mathbf{B}$  is an  $M \times 1$  vector and composed by  $M$  times of measurement, that is  $\mathbf{B} = [B^{(1)}, B^{(2)}, \dots, B^{(M)}]^T$ . Similarly,  $\mathbf{O}$  is an  $M \times 1$  vector made up of the reflection coefficient  $O(x, y)$  of object,  $\mathbf{O} = [O(1, 1), O(1, 2), \dots, O(p, q)]^T$ . In addition,  $\Psi = \Phi - I\langle\Phi\rangle$ ,  $\Phi \mathbf{O} = \mathbf{B}$ , and  $\langle \mathbf{B} \rangle = \langle \Phi \rangle \mathbf{O}$ .  $\mathbf{I}$  represents an  $M \times 1$  column vector of all elements with a value of 1.  $\langle \Phi \rangle$  is a  $1 \times N$  row vector, which denotes the average of each column of  $\Phi$ . Theoretically, a high quality reconstructed image will be obtained by Eq. 3, if  $\Psi^T \Psi$  is a diagonal matrix. And in CGI system, the full-width at half maximum of  $\Psi^T \Psi$  diagonal nonzero elements determines the spatial transverse resolution of the preset light field [21], which is proportional to the resolution on the object plane. Hence, to realize the multi-resolution progressive computational ghost imaging, a multi-resolution  $\Psi^T \Psi$  with different measurements number is extremely essential.

### 2.2. Reordering methods for Hadamard derived pattern

To enable high-speed multi-resolution progressive computational ghost imaging, we optimized the sequence of Hadamard derivative pattern to achieve real-time high-resolution imaging. Then, we will show how to select and use Hadamard derived pattern to actualize the multi-resolution progressive imaging.

The Hadamard basis is a square matrix composed of  $+1$  and  $-1$ , and can be generated rapidly by Kronecker product, that is

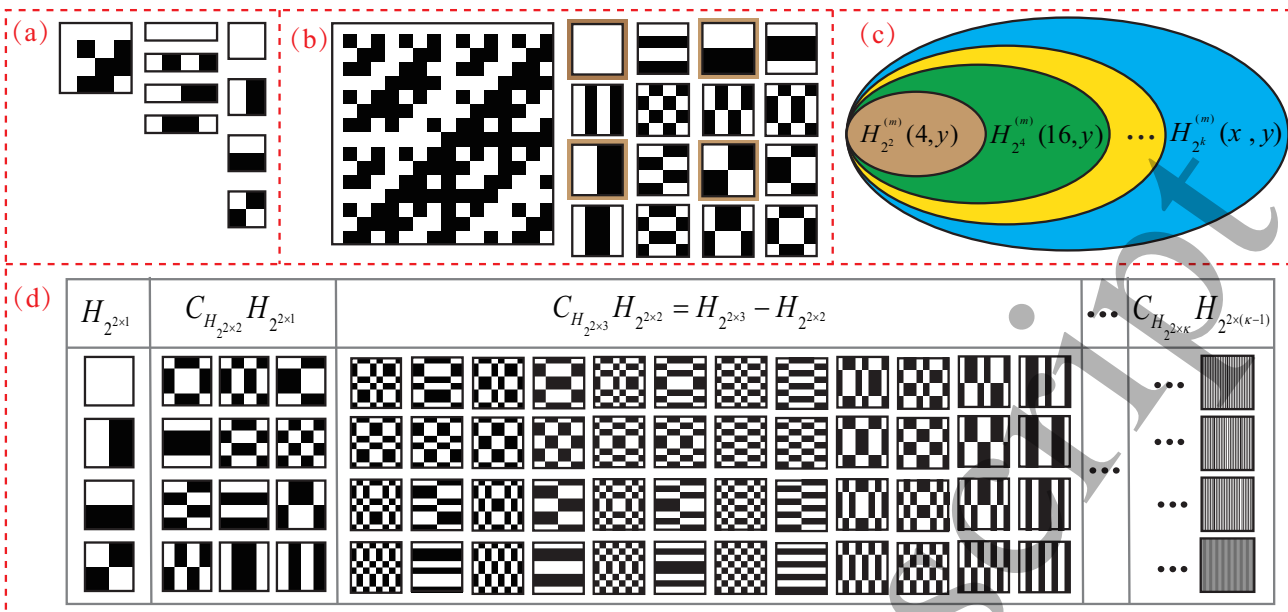
$$\begin{cases} H_{2^1} = \begin{bmatrix} +1 & +1 \\ +1 & -1 \end{bmatrix}, \\ H_{2^k} = H_{2^1} \otimes H_{2^{k-1}} = \begin{bmatrix} +H_{2^{k-1}} & +H_{2^{k-1}} \\ +H_{2^{k-1}} & -H_{2^{k-1}} \end{bmatrix}, \end{cases} \quad (4)$$

where  $2 < k$  (integer), and  $\otimes$  denotes the Kronecker product. Hence, a Hadamard matrix of size  $M \times N$  ( $M = N$ ),

$$H_{2^k}(m, n) = \begin{bmatrix} H(1, 1) & H(1, 2) & \cdots & H(1, N) \\ H(2, 1) & H(2, 2) & \cdots & H(2, N) \\ \vdots & \vdots & \ddots & \vdots \\ H(M, 1) & H(M, 2) & \cdots & H(M, N) \end{bmatrix}. \quad (5)$$

To construct a modulation matrix of the light field for GI, we will select an arbitrary row of  $H_{2^k}(m, n)$  to obtain a two-dimensional Hadamard derived pattern  $H_{2^k}^{(m)}(x, y)$ .

To get a set of Hadamard derived pattern  $H_{2^k}^{(m)}(x, y)$ , we first generate a high-order Hadamard matrix  $H_{2^k}(m, n)$  that can satisfy the imaging resolution [taking  $k = 2$  for example, as shown in the left panel of Fig. 2(a)]. Then, we extract each row of  $H_{2^k}(m, n)$  to obtain the corresponding single row



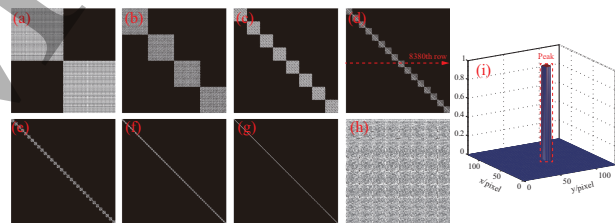
**Figure 2.** (Color online) Reordering methods for Hadamard derived pattern. (a) Hadamard derived pattern of order four construction process; (b) Hadamard pattern of order eight and the corresponding derived pattern; (c) Hadamard derived pattern of different order sets; (d) Reordered Hadamard derived pattern.

vectors[as shown in the middle panel of Fig. 2(a)]. At last, we acquire the two-dimensional matrix  $H_{2^k}^{(m)}(x,y)$  of  $x$  rows and  $y$  columns. (Starting) from the top (all the way) down to the bottom of the columns in the right extreme in Fig. 2(a), we give the derived pattern  $H_{2^2}^{(m)}(2,2)$  with  $m = 1, 2, 3, 4$ , respectively.

Since the Hadamard matrix is a direct product of  $H_{2^1}$ , the higher order Hadamard matrix naturally contains the distribution information of lower order Hadamard matrix. For example, with  $k = 4$ , the 16pixel  $\times$  16pixel Hadamard pattern  $H_{2^4}(16,16)$  is shown in the left subfigure of Fig. 2(b). The corresponding Hadamard derived pattern in the right subfigure Fig. 2(b) contains the 4-order Hadamard derived matrix  $H_{2^2}^{(m)}(4,4)$ , which is labelled by brown frames. For the purpose of reordering, we enlarge the latter matrix to the same size as the former one. In a similar derived approach, every pattern  $H_{2^k}^{(m)}(x,y)$  is a proper subset of the  $H_{2^{k'}}^{(m)}(x,y)$  for  $k' > k$ , and the relationship between the sets is shown in Fig. 2(c).









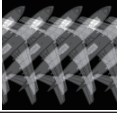






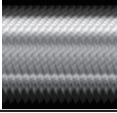


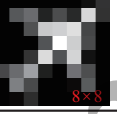

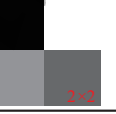


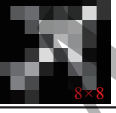

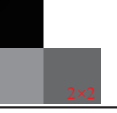
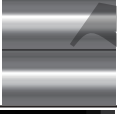


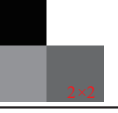
With the lower and higher derived pattern in our hand, we are now ready to reorder them. For a high order derived pattern  $H_{2^k}^{(m)}(x,y)$ ,  $k = 2 \times \kappa$ , we first extract the lowest order derived pattern, i.e.,  $H_{2^{2 \times 1}}^{(m)}(2,2)$  and propose it. Then, extract hadamard derived patterns of order 16 [ $H_{2^{2 \times 2}}^{(m)}(4,4)$ ] from the remaining Hadamard derived patterns [ $H_{2^{2 \times \kappa}}^{(m)}(x,y) -$

$H_{2^{2 \times 1}}^{(m)}(2,2)$ ] and place it behind the previously extracted derived patterns [ $H_{2^{2 \times 1}}^{(m)}(2,2)$ ], and deal with the rest lower order patterns [ $H_{2^{2 \times 3}}^{(m)}(8,8), H_{2^{2 \times 4}}^{(m)}(16,16), H_{2^{2 \times 5}}^{(m)}(32,32), \dots, H_{2^{2 \times (\kappa-1)}}^{(m)}$ ] according to priority in the same way.



**Figure 3.** (Color online) Comparison of the full-widths at half-maximum of  $\Psi^T \Psi$  with different measurements number. (a)  $M = 2^{2 \times 1}$  ( $2 \times 2$  resolution); (b)  $M = 2^{2 \times 2}$  ( $4 \times 4$  resolution); (c)  $M = 2^{2 \times 3}$  ( $8 \times 8$  resolution); (d)  $M = 2^{2 \times 4}$  ( $16 \times 16$  resolution); (e)  $M = 2^{2 \times 5}$  ( $32 \times 32$  resolution); (f)  $M = 2^{2 \times 6}$  ( $64 \times 64$  resolution); (g)  $M = 2^{2 \times 7}$  ( $128 \times 128$  resolution); (h) Reordered Hadamard pattern; (i) the data in the 8380th row of the matrix (d) is reshaped as a 128pixel  $\times$  128pixel image.

Concretely, in the language of the sets theory,  $H_{2^{2 \times 1}}$  is a proper subset of  $H_{2^{2 \times 2}}$  which is notated as  $H_{2^{2 \times 1}} \subsetneq H_{2^{2 \times 2}}$  [to make it simple, we omit the superscript  $m$  in what follows], and the complementary set as  $C_{H_{2^{2 \times 2}}} H_{2^{2 \times 1}} = H_{2^{2 \times 2}} - H_{2^{2 \times 1}}$ , which is shown by the green area in Fig. 2(c). As for the higher order, every two adjacent even orders will produce a corresponding complementary set  $C_{H_{2^{2 \times \kappa}}} H_{2^{2 \times (\kappa-1)}} = H_{2^{2 \times \kappa}} - H_{2^{2 \times (\kappa-1)}}$ , whose elements will be reordered in our scheme[as shown in Fig. 2(d)]. In a word,

Measurement times	Imaging scheme	Reconstructed multi-resolution images ( $m \times n$ resolution)
16384 ( $M=2^{2^7}$ )	TCGI	
	MPCGI	      
4096 ( $M=2^{2^6}$ )	TCGI	
	MPCGI	     
1024 ( $M=2^{2^5}$ )	TCGI	
	MPCGI	    
256 ( $M=2^{2^4}$ )	TCGI	
	MPCGI	   
64 ( $M=2^{2^3}$ )	TCGI	
	MPCGI	  

**Figure 4.** (Color online) Numerical simulation experimental results of TCGI and MPCGI schemes with different measurement times.

by enlarging the complementary set constantly we completed the Hadamard derived pattern reordering,  $H_{2^k}^{(m)}(x, y)_{\text{new}}$ , and the two dimensional form can be expressed as  $\mathbf{H}_{2^k}(\mathbf{m}, \mathbf{n})_{\text{new}}$  which is equivalent to  $\Phi$  in Eq. 2. At this point,  $\Psi = \mathbf{H}_{2^k}(\mathbf{m}, \mathbf{n})_{\text{new}} - \mathbf{I}(\mathbf{H}_{2^k}(\mathbf{m}, \mathbf{n})_{\text{new}})$ , the different full-widths at half-maximum of  $\Psi^T \Psi$  with different measurements number  $M = 2^{2^{\kappa}} (\kappa = 1, 2, \dots)$  can be efficiently calculated, as shown in Fig. 3. If the data in the 8380th row of the matrix Fig. 3(d) is reshaped as a 128pixel  $\times$  128pixel image, as displayed in Fig. 3(i), the full-width at half-maximum of the

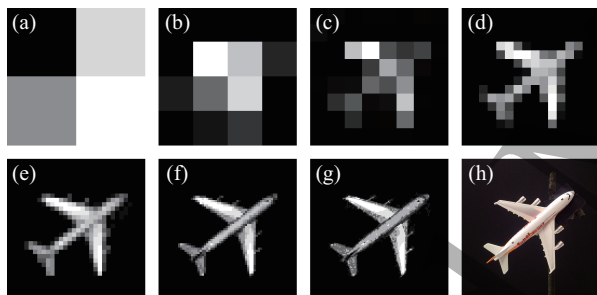
peak image determines the spatial transverse resolution of GI [21]. So, as can be seen from Fig. 3(a)-(g), we can get seven different full-width at half-maximum images when  $M = 2^{2^{\kappa}}$ . Hence, we can achieve the multi-resolution progressive progressive imaging quickly.

To demonstrate the advantages of this method, we select an aircraft image with the image size of 128pixel  $\times$  128pixel as the target object for numerical simulation experimental. The comparison results with traditional computational ghost imaging (TCGI) using natural

order Hadamard derived pattern are shown in Fig. 4. By comparing the results TCGI and MPCGI in Fig. 4, it is noteworthy that the MPCGI can obtain 3, 4, 5, 6 and 7 multi-resolution images respectively when the measurement times is 64 ( $M = 2^{2 \times 3}$ ), 256 ( $M = 2^{2 \times 4}$ ), 1024 ( $M = 2^{2 \times 5}$ ), 4096 ( $M = 2^{2 \times 6}$ ), 16384 ( $M = 2^{2 \times 7}$ ). Obviously, the MPCGI can obtain  $\kappa$  images with different resolutions when the measurement times are  $M = 2^{2 \times \kappa}$ ,  $\kappa = 1, 2, 3, \dots$ . With this, continuous multi-resolution imaging is realized. The results also show that this scheme can be used for imaging at low measurement times. For example, MPCGI method can perform low-resolution imaging on the target object of 128pixel  $\times$  128pixel when  $M = 2^{2 \times 4}$ , but TCGI did not.

### 3. Experimental results

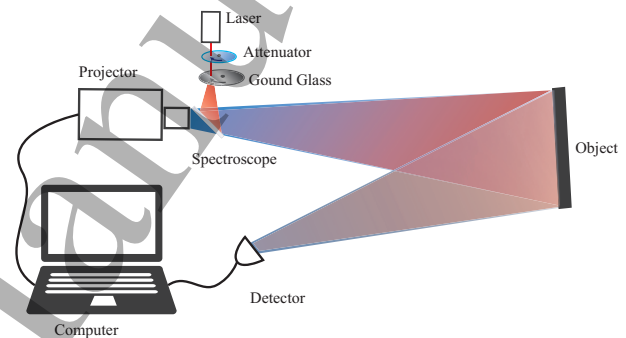
To verify the feasibility of MPCGI, we conducted a series of experiments. In the experiments, the object is an aircraft model [see Fig. 5(h)] with the size of 20cm  $\times$  17cm and positioned about 0.72 m, 2.42 m away from the projector (XGIMI Z4 Air miniature projector) and bucket detector (Thorlabs, PDA100A-EC, 320-1100 nm, 2.4 MHz BW, 100 mm<sup>2</sup>), respectively.



**Figure 5.** Multi-resolution progressive computational ghost imaging results. (a)  $M = 2^{2 \times 1}$  ( $2 \times 2$  resolution); (b)  $M = 2^{2 \times 2}$  ( $4 \times 4$  resolution); (c)  $M = 2^{2 \times 3}$  ( $8 \times 8$  resolution); (d)  $M = 2^{2 \times 4}$  ( $16 \times 16$  resolution); (e)  $M = 2^{2 \times 5}$  ( $32 \times 32$  resolution); (f)  $M = 2^{2 \times 6}$  ( $64 \times 64$  resolution); (g)  $M = 2^{2 \times 7}$  ( $128 \times 128$  resolution); (h) Original object.

We adopted a set of reordered Hadamard derived pattern  $H_{2^{2 \times 7}}^{(m)}(128, 128)_{\text{new}}$ ,  $m = 1, 2, 3, \dots, 16384$ , i.e., we have done a set of seven resolutions MPCGI experiments and the results are shown in Fig. 5. With the increase of the number of the measurements, the aircraft image information of the reconstructed image gradually becomes clear, i.e., image resolution steadily increased with measurement times. When the imaging resolution of MPCGI is  $4 \times 4$  [Fig. 5 (b)  $M = 2^{2 \times 2}$ ], the position of the target object can be clearly identified. Hence, the target location can be locked

by a low-resolution image with a small number of measurements. Even for  $M = 2^{2 \times 5}$  ( $32 \times 32$  resolution), we can clearly distinguish the clear outline of the target object (an aircraft), which is enough for the military reconnaissance. As the number of measurements is further increased, the details of the reconstructed image gradually emerge. For example, the engines on both sides of the aircraft have been reconstructed by measuring  $2^{2 \times 6}$  times, as shown in Fig. 5(f). To achieve the same efficiency, 5460 times are needed in the TCGI scheme. Hence, 1364 measurement times can be reduced by our MPCGI scheme. Furthermore, after a 4-fold increase in resolution, we find out that the reconstructed image Fig. 5(g) is much the same with Fig. 5(f), which shows that, in a few cases, high imaging resolution is indispensable to CGI, but there is a waste of resources in ultra-high imaging resolution. The results of MPCGI experiments verify the feasibility of the multi-resolution progressive imaging and low resolution location.



**Figure 6.** (Color online) Schematic diagram of computational ghost imaging under background light noise.

To evaluate the performance of our scheme under background light noise, we introduce the detection signal-to-noise ratio (DSNR) which is defined as

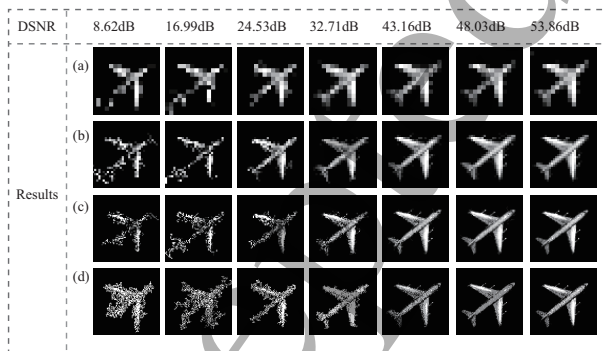
$$DSNR = 10 \log_{10} \frac{\langle B \rangle}{\sqrt{\langle (E - \langle E \rangle)^2 \rangle}}, \quad (6)$$

where  $\langle B \rangle$  is the mean signal power and  $\langle E \rangle$  is the mean background light noise power [22]. For the 16384 measurements [Fig. 5], the DSNR is close to positive infinity (without noise), which exceeds the criterion in applicable practical application scenarios. Therefore, we add a laser and modulate it by a rotating ground glass (as shown in Fig. 6), and we weaken the intensity of the laser by attenuator to get different DSNR so as to discuss the multi-resolution progressive imaging performance of the proposed scheme.

In Fig. 7, we show MPCGI results for different DSNR and resolution (equal to the measurement times). In the low DSNR case ( $DSNR < 32.71 \text{ dB}$ ), the low-resolution images

can be effectively reconstructed [Fig. 7(a)-(b)]. Unlike low resolution imaging, the high-resolution imaging can only get blurred reconstructed images [Fig. 7(c)-(d)]. And if the DSNR is too low ( $\text{DSNR} < 8.62\text{dB}$ ), the experimental system will be invalid. By contrast, when the DSNR is high enough ( $\text{DSNR} > 32.71\text{dB}$ ), the method can effectively reconstruct the multi-resolution images [Fig. 7(a)-(d)], and it has fine image formation ability. And when the DSNR is  $53.86\text{dB}$ , the image quality with  $M = 16384$  [Fig. 7(d)  $128 \times 128$  resolution] and  $M=4096$  [Fig. 7(c)  $64 \times 64$  resolution] are almost equal in vision. The results show that high-resolution images are difficult to obtain at low DSNR (i.e., the greater the resolution, the worse the noise resistance). When the DSNR is sufficient and there is no big demand for high-resolution, a large number of measurement times are not required to obtain the higher resolution images. Simultaneously, we find that a higher resolution is combined with a high DSNR for an ideal image reconstruction, and low resolution imaging robust performance is superior to high resolution. Moreover, a high resolution imaging is still the optimal choice in the case of high DSNR.

In the GI experiment, some evaluation indicators (such as signal-to-noise ratio, visibility, contrast to noise ratio, etc.) require the target image information and reconstructed image after a large number of measurements, and it makes the obtained reference evaluation values lag behind. In contrast, DSNR can be directly calculated based on the echo signal power and background light noise power received by the detector and the image information of the target object is not required. Because of that, we can refer to the DSNR to analyze whether the experimental echo signal power meets the imaging requirements in advance.



**Figure 7.** Results of different DSNR. (a)  $M = 2^{2 \times 4}$  ( $16 \times 16$  resolution); (b)  $M = 2^{2 \times 5}$  ( $32 \times 32$  resolution); (c)  $M = 2^{2 \times 6}$  ( $64 \times 64$  resolution); (d)  $M = 2^{2 \times 7}$  ( $128 \times 128$  resolution).

#### 4. Conclusion

In this paper, we have proposed and demonstrated a new method named multi-resolution progressive computational ghost imaging which uses the Hadamard derived pattern to realize continuous multi-resolution imaging simply and quickly. Both numerical simulations and experimental realizations have been used to demonstrate its exceptional features. First of all, continuous multi-resolution images can be retrieved without additional detection; second, the number of measurements is much less than for TCGI scheme; third, the complexity of Hadamard derived pattern reordering and multi-resolution imaging implementation is greatly reduced, compared with “Russian Dolls” ordering of the Hadamard [19] method; fourth, studies on the effect of DSNR for different resolution can provide some reference value for practical application. Furthermore, if the order of hadamard can be further optimized and the ultra high speed spatial light modulator (such as digital micromirror devices or LED-array [23]) is used, the MPCGI method can approximate the real-time imaging requirements of video frame rate. In some practical application scenarios like ground-to-air or air-to-air imaging, especially air surveillance applications, it is necessary to quickly feedback the results of target detection and recognition based on the feature information of multi-resolution images. In this case, the MPCGI method can play an key role.

#### Funding

This work is supported by the Project of the Science and Technology Department of Jilin Province (Grant No. 20170204023GX); the Special Funds for Provincial Industrial Innovation in Jilin Province (Grant No. 2018C040-4, 2019C025); Youth Innovation Promotion Association of the Chinese Academy of Sciences; and the Young Foundation of Science and Technology Department of Jilin Province (Grant No. 20170520109JH).

#### Acknowledgments

We thank Z. H. Wang, G. C. Wang, A. J. Sang and X. F. An for their fruitful discussions.

#### References

- [1] Pittman T B, Shih Y H, Strekalov D V and Sergienko A V 1995 Optical imaging by means of two-photon quantum



- entanglement *Phys. Rev. A* **52** R3429-R3432
- [2] Gatti A, Brambilla E, Bache M and Lugiato L A 2004 Ghost imaging with thermal light: Comparing entanglement and classical correlation *Phys. Rev. Lett.* **93** 093602
- [3] Zhao C, Gong W, Chen M, Li E, Wang H, Xu W and Han S 2012 Ghost imaging lidar via sparsity constraints *Appl. Phys. Lett.* **101** 141123
- [4] Gong W, Zhao C, Yu H, Chen M, Xu W and Han S 2016 Three-dimensional ghost imaging lidar via sparsity constraint *Sci. Rep.* **6** 26133
- [5] Gong W and Han S 2015 High-resolution far-field ghost imaging via sparsity constraint *Sci. Rep.* **5** 9280
- [6] Gong W and Han S 2012 Experimental investigation of the quality of lensless super-resolution ghost imaging via sparsity constraints *Phys. Lett. A* **376** 1519-1522
- [7] Clemente P, Durn V, Torres-Company V, Tajahuerce E and Lancis J 2010 Optical encryption based on computational ghost imaging *Opt. Lett.* **35** 2391-2393
- [8] Shapiro J H 2008 Computational ghost imaging *Phys. Rev. A* **78** 061802
- [9] Bromberg Y, Katz O, and Silberberg Y 2009 Ghost imaging with a single detector *Phys. Rev. A* **79** 053840
- [10] Katz O, Bromberg Y and Silberberg Y 2009 Compressive ghost imaging *Appl. Phys. Lett.* **95** 131110
- [11] Du J, Gong W, Han S 2012 The influence of sparsity property of images on ghost imaging with thermal light *Opt. Lett.* **37** 1067C1069
- [12] Yu H, Li E, Gong W, Han S 2015 Structured image reconstruction for three-dimensional ghost imaging lidar *Opt. Express* **23** 14541C14551
- [13] Gong W, Yu H, Zhao C, Bo Z, Chen M, and Xu W 2016 Improving the imaging quality of ghost imaging lidar via sparsity constraint by time-resolved technique *Remote Sens.* **8** 991
- [14] Averbuch A, Dekel S and Deutsch S 2012 Adaptive compressed image sensing using dictionaries *SIAM Journal on Imaging Sciences* **5** 57-89
- [15] Aßmann M and Bayer M 2013 Compressive adaptive computational ghost imaging *Sci. Rep.* **3** 1545
- [16] Yu W K *et al.* 2014 Adaptive compressive ghost imaging based on wavelet trees and sparse representation *Opt. Express* **22** 7133C7144
- [17] Soldevila F, Salvador-Balaguer E, Clemente P, Tajahuerce E and Lancis J 2015 High-resolution adaptive imaging with a single photodiode *Sci. Rep.* **5** 14300
- [18] Phillips D B, Sun M J, Taylor J M, Edgar M P, Barnett S M, Gibson G M and Padgett M J 2017 Adaptive foveated single-pixel imaging with dynamic supersampling *Sci. Adv.* **3** e1601782
- [19] Sun M J, Meng L T, Edgar M P, Padgett M J and Radwell N 2017 A russian dolls ordering of the hadamard basis for compressive single-pixel imaging *Sci. Rep.* **7** 3464
- [20] Christopoulos C, Skodras A and Ebrahimi T 2000 The jpeg2000 still image coding system: an overview *Consumer Electron. IEEE Transactions on* **46** 1103-1127
- [21] Wang C, Gong W, Shao X and Han S 2016 The influence of the property of random coded patterns on fluctuation-correlation ghost imaging *J. Opt.* **18** 065703
- [22] Deng C, Pan L, Wang C, Gao X, Gong W and Han S 2017 Performance analysis of ghost imaging lidar in background light environment *Photon. Res.* **5** 431-435
- [23] Xu Z H, Chen W, Penuelas J, Padgett M and Sun M J 2018 1000 fps computational ghost imaging using led-based structured illumination *Opt. Express* **26** 2427-2434